

TELAMON: TeV Effelsberg Long-term AGN Monitoring

I. Program description and sample characterization

F. Eppel^{1,2}, M. Kadler¹, J. Heßdörfer^{1,2}, P. Benke^{2,1}, L. Debbrecht², J. Eich¹, A. Gokus^{3,4}, S. Hämmerich⁴, D. Kirchner¹, G. F. Paraschos², F. Rösch^{1,2}, W. Schulga¹, J. Sinapius⁵, P. Weber¹, U. Bach², D. Dorner¹, P. G. Edwards⁶, A. Kraus², O. Hervet⁷, S. Koyama⁸, T. P. Krichbaum², K. Mannheim¹, E. Ros², M. Zacharias⁹, and J. A. Zensus²

¹ Julius-Maximilians-Universität Würzburg, Institut für Theoretische Physik und Astrophysik, Lehrstuhl für Astronomie, Emil-Fischer-Straße 31, D-97074 Würzburg, Germany
e-mail: florian.eppel@uni-wuerzburg.de

² Max-Planck-Institut für Radioastronomie, Auf dem Hügel 69, D-53121 Bonn, Germany

³ McDonnell Center for Space Science, Washington University, MSC 1105-109-03, One Brookings Drive, St. Louis, MO 63130-4899, USA

⁴ Remeis Observatory and Erlangen Centre for Astroparticle Physics, Universität Erlangen-Nürnberg, Sternwartstr. 7, 96049 Bamberg, Germany

⁵ Deutsches Elektronen-Synchrotron DESY, Platanenallee 6, 15738 Zeuthen, Germany

⁶ CSIRO Astronomy and Space Science, ATNF, PO Box 76, Epping NSW 1710, Australia

⁷ Santa Cruz Institute for Particle Physics and Department of Physics, University of California, Santa Cruz, CA 95064, USA

⁸ Niigata University, 8050 Ikarashi-nino-cho, Nishi-ku, Niigata 950-2181, Japan

⁹ Landessternwarte, Universität Heidelberg, Königsstuhl, D-69117 Heidelberg, Germany

Received October XX, 2023; accepted Month XX, 2023

ABSTRACT

Aims. We introduce the TELAMON program which is using the Effelsberg 100-m telescope to monitor the radio spectra of active galactic nuclei (AGN) under scrutiny in astroparticle physics, specifically TeV blazars and candidate neutrino-associated AGN. Here, we present and characterize our main sample of TeV-detected blazars.

Methods. We analyze the data sample from the first ~2.5 years of observations between August 2020 and February 2023 in the range from 14 GHz to 45 GHz. During this pilot phase, we have observed all 59 TeV-detected blazars in the Northern Hemisphere (i.e., Dec. $> 0^\circ$) known at the time of observation. We discuss the basic data reduction and calibration procedures used for all TELAMON data and introduce a sub-band averaging method used to calculate average light curves for the sources in our sample.

Results. We find that the TeV-selected sources in our sample exhibit a median flux density of 0.12 Jy at 20 mm, 0.20 Jy at 14 mm and 0.60 Jy at 7 mm. The spectrum for most of the sources is consistent with a flat radio spectrum and we find a median spectral index ($S(\nu) \propto \nu^\alpha$) of $\alpha = -0.11$. Our results on flux density and spectral index are consistent with previous studies of TeV-selected blazars. Compared to the GeV-selected F-GAMMA sample, TELAMON sources are significantly fainter in the radio band. This is consistent with the idea of the blazar sequence that the double-humped spectrum of blazars is shifted towards higher frequencies for TeV-emitters (in particular for HBLs), which results in a lower radio flux density. We do not find significant differences between our TeV-selected blazar sample and the GeV-selected F-GAMMA sample in terms of the spectral index distribution. Moreover, we present a strategy to track the light curve evolution of sources in our sample for a variability and correlation analysis which we plan for the future.

Key words. blazars – TeV – jetted AGN – radio

1. Introduction

Blazars are radio-loud active galactic nuclei (AGN) hosting relativistic jets pointed close to our line of sight. Their emission is highly beamed and Doppler-boosted, which makes them variable broadband emitters from radio to γ -ray energies. Their spectral energy distribution (SED) typically shows a two-peaked (double-humped) spectrum. The first peak corresponds to synchrotron emission while the second peak is often attributed to inverse Compton scattering. High-synchrotron peaked BL Lac type objects (HBLs) are defined as sources whose primary (synchrotron) emission hump peaks above 10^{15} Hz in νF_ν scale (Padovani & Giommi 1995). In the most extreme cases, they peak at even higher frequencies by up to two orders of magnitude for the so called extreme HBLs (EHBLs, Ghisellini 1999; Biteau

et al. 2020). The second, high-energy peak of blazar SEDs can stretch into the very-high-energy (VHE) regime at TeV γ -rays. Imaging Air Cherenkov Telescopes have been able to detect VHE emission from ~80 blazars, with the majority of them being HBLs¹. Most of these sources are faint radio sources, which makes TeV-emitting blazars difficult to study in the radio band. Blazars are of utmost interest for astroparticle physics as potential sources of ultrahigh-energy cosmic rays and neutrinos (e.g., Hillas 1984; Mannheim 1995). In particular, HBLs and EHBLs have been considered in some recent theoretical works as relevant neutrino sources (Tavecchio et al. 2014; Padovani et al. 2015; Giommi et al. 2020). We have established the TeV Effelsberg Long-term AGN Monitoring (TELAMON) program in

¹ <http://tevcat2.uchicago.edu>

August 2020, a radio monitoring program which uses the Effelsberg 100-m telescope to investigate the radio properties of TeV-emitting blazars. We perform radio observations of a sample of TeV-selected blazars at high frequencies up to 44 GHz to trace dynamical process in these objects. Our program is designed to monitor the radio spectra of TeV-blazars and candidate neutrino AGN. A first study of TeV-selected HBLs and EHBLs has been presented by Lindfors et al. (2016) at 15 GHz. We extend their observations with radio coverage at multiple frequencies, and, for the first time, a spectral characterization of these objects. In Section 2, we explain in detail the sample selection and observing setup used with the Effelsberg 100-m telescope. On top of that, we present the TELAMON analysis pipeline including cross-scan setup and calibration procedures. In Section 3, we present first results for sources in our sample and present average flux densities and spectral indices for all observed sources. These results are discussed and compared with previous studies, e.g., the Lindfors et al. (2016) study, in Section 4. Moreover, we compare source properties of the TeV-selected sources in our sample with the GeV-selected F-GAMMA (Fuhrmann et al. 2016; Angelakis et al. 2019) sample and discuss similarities and differences. In Section 5, we give an overview about planned future publications and the overall relevance of the TELAMON project within current developments in astroparticle physics.

2. Observations & analysis

2.1. Program description & sample

Our sample consists of all 59 TeV-detected blazars² in the Northern Hemisphere (i.e., Dec. $> 0^\circ$). In addition, we include 5 TeV-detected blazars from the Southern Hemisphere and a TeV-detected radio galaxy (3C 264) as sources of special interest. This TeV-selected sample, consisting of 65 sources, is presented in Table 1. It includes 28 EHBLs (i.e., $\nu_{\text{peak}} \geq 10^{17}$ Hz, and sources from Biteau et al. 2020), 19 HBLs (i.e., 10^{15} Hz $\leq \nu_{\text{peak}} < 10^{17}$ Hz), 5 intermediate-peaked BL Lac type objects (IBL, i.e., 10^{14} Hz $\leq \nu_{\text{peak}} < 10^{15}$ Hz), 4 low-peaked BL Lac type objects (LBL, i.e., $\nu_{\text{peak}} < 10^{14}$ GHz), 8 flat-spectrum radio quasars (FSRQ) and 1 Radio Galaxy (RG). For J0316+4119 (IC 310), a clear characterization is not yet possible since the source shows some blazar-like properties but its jet might be misaligned by 10–20° from the line of sight (Ahnen et al. 2017). We include the source in our EHBL count, according to its peak frequency found in the literature. Note that Biteau et al. (2020) further distinguishes the EHBL class into three different types, according to their distinct extreme behavior. In our analysis, we label all 18 overlapping sources with Biteau et al. (2020) as EHBL. Moreover, we have identified 10 additional sources as EHBL in our sample according to their high synchrotron-peak frequency found in the literature, which were not included in Biteau et al. (2020) (cf. Table 1).

2.2. Observations

For our observations, we are using the Effelsberg 100-m telescope operated by the Max-Planck-Institute for Radio Astronomy in Bonn, Germany. The observations presented here are conducted with the 20 mm, 14 mm and 7 mm receivers mounted in the secondary focus, in continuum observing mode with the backend “dual-spec-OPTOCBE”. This results in four sub-bands (centered at 19.25 GHz, 21.15 GHz, 22.85 GHz and

24.75 GHz) for the 14 mm receiver, and four sub-bands (centered at 36.25 GHz, 38.75 GHz, 41.25 GHz, 43.75 GHz) for the 7 mm receiver, which we are using since August 2020. Since spring 2021, the 20 mm receiver has been added yielding two additional frequency bands (centered at 14.25 GHz and 16.75 GHz). Note that we also started using the “SpecPol” receiver backend to record polarization information at the same time (cf. Heßdörfer et al. 2023). The polarization analysis and first results will be assessed in a separate publication. All receivers are equipped with two horns. The first horn is pointed directly at the target and passes the signal directly to the receiver. The second horn is pointed at the atmosphere off-source and is used to subtract weather effects from the first horn. We apply this weather subtraction to all of our observations, because at the used frequencies Earth’s atmosphere (especially on cloudy days) emits thermal radiation that needs to be accounted for. In order to measure the flux density of a source, “cross-scans” are performed on the targets, consisting of typically 8 sub-scans (4 in azimuth and 4 in elevation) at 20 mm, 14 mm and 7 mm (36.25 GHz, 38.75 GHz). For the higher 7 mm frequencies (41.25 GHz, 43.75 GHz), 16 sub-scans (8 in azimuth and 8 in elevation) are used. During a cross-scan the telescope slews over the point-like source region in azimuth- and elevation-direction multiple times while measuring the antenna temperature of the receiver. About every four hours, a calibrator source is observed in order to focus the telescope and to extract calibration factors (cf. Sect. 2.4).

For this work, we consider all observations from within the first 2.5 years of the program, i.e., from August 2020 to February 2023. This comprises data taken in 95 observing sessions (epochs) with a total observing time of 1160.3 hours. Note that part of the observing time was also used for observations of neutrino-candidate sources, which will be discussed in a separate publication (cf. Kadler et al. 2021). During this time, we have observed 65 distinct TeV-sources in total, 53 at 20 mm, 61 at 14 mm and 45 at 7 mm. In order to select the statistically most complete sample from our observed targets, we will from here on only address the 59 Northern (i.e., Dec. $> 0^\circ$) TeV-blazars. Results for the 5 Southern sources and the radio galaxy 3C 264 (J1145+1936) are presented in Appendix B. Plots of the latest available light curves and spectra are publicly available on the dedicated TELAMON website³.

2.3. Data acquisition & reduction

The general data analysis for pointed flux density measurements with the Effelsberg 100-m telescope has been described in detail by Angelakis et al. (2019) in context of the F-GAMMA program. We use a very similar data reduction procedure and will therefore restrict this section to the changes and improvements compared to the analysis of Angelakis et al. (2019). The major improvements presented here are a semi-automated flagging algorithm, a new calibration procedure, and an in-depth measurement uncertainty discussion. In principle, this section explains how the raw data output of every scan, namely antenna temperatures, is converted into astrophysical units of jansky. The antenna temperatures are calculated by using a noise diode switching system (cf. Müller et al. 2017). Left-handed circular polarization (LCP) and right-handed circular polarization (RCP) are averaged.

² <http://tevcat2.uchicago.edu>

³ <https://telamon.astro.uni-wuerzburg.de/>

Table 1: The TELAMON sample of TeV-emitting AGN. The classification into EHBL, HBL, IBL and LBL is performed according to the synchrotron peak frequency found in the literature. The presented references are related to the synchrotron peak frequency and the redshift value.

ID (J2000)	Alternative Name	Class	Synchr. Peak $\log_{10} \left(\frac{\nu_{\text{peak}}}{\text{Hz}} \right)$	Redshift ^a	Reference
J0035+5950	1ES 0033+595	EHBL	18.2	0.086	Chang et al. (2019)
J0112+2244	S2 0109+22	IBL	~ 15	0.4	Ciprini et al. (2004)
J0136+3906	RGB J0136+391	HBL	~16	0.2	Costamante & Ghisellini (2002)
J0152+0146*	RGB J0152+017	EHBL	17	0.080	Aharonian et al. (2008)
J0214+5144*	TXS 0210+515	EHBL	17.3	0.049	Chang et al. (2019)
J0221+3556	S3 0218+35	FSRQ	-	0.954	Paiano et al. (2017)
J0222+4302	3C 66A	HBL	15.63	0.34	Nieppola et al. (2006)
J0232+2017*	1ES 0229+200	EHBL	18.5	0.139	Chang et al. (2019)
J0303-2407	PKS 0301-243	HBL	15.7	0.266	Chang et al. (2019)
J0316+4119	IC 310	RG/EHBL	17	0.0189	Ahnen et al. (2017)
J0319+1845	RBS 0413	EHBL	17.3	0.19	Chang et al. (2019)
J0416+0105*	1ES 0414+009	EHBL	16.5	0.287	Chang et al. (2019)
J0507+6737	1ES 0502+675	EHBL	17.9	0.34	Chang et al. (2019)
J0509+0541	TXS 0506+056	HBL	15.34	0.3365	Nieppola et al. (2006)
J0521+2112	RGB J0521+212	IBL	15.1	0.108	Chang et al. (2019)
J0648+1516	RX J0648.7+1516	HBL	> 16	0.179	Aliu et al. (2011)
J0650+2502	1ES 0647+250	HBL	16.7	0.203	Chang et al. (2019)
J0710+5909*	RGB J0710+591	EHBL	18.1	0.12	Chang et al. (2019)
J0721+7120	S5 0716+714	IBL	~14.5	-	Giommi et al. (1999)
J0733+5153*	PGC 2402248	EHBL	17.9	0.09	Chang et al. (2019)
J0739+0136	[HB89] 0736+017	FSRQ	-	0.18941	Grasha et al. (2019)
J0809+5219	1ES 0806+524	HBL	16.6	0.138	Aleksić et al. (2011)
J0812+0237	1RXS J081201.8+023735	EHBL	17.5	0.1721	Ventura et al. (2021)
J0847+1133*	RBS 0723	EHBL	17.8	0.198	Chang et al. (2019)
J0854+2006†	OJ287	LBL	13.4	0.306	Abdo et al. (2010)
J0913-2103	MRC 0910-208	EHBL	17.1	0.198	Chang et al. (2019)
J0958+6533	S4 0954+658	FSRQ	-	0.3694	Becerra González et al. (2021)
J1015+4926	1ES 1011+496	HBL	16.4	0.2	Chang et al. (2019)
J1058+2817	GB6 J1058+2817	EHBL	18.37	0.4793	Nieppola et al. (2006)
J1104+3812*	Mrk 421	EHBL	16.3	0.03	Chang et al. (2019)
J1136+7009	Mrk 180	HBL	16.8	0.045	Chang et al. (2019)
J1136+6737*	RX J1136.5+6737	EHBL	18.1	0.134	Chang et al. (2019)
J1145+1936	3C 264	RG	-	0.0216	Ahn et al. (2012)
J1159+2914	4C+29.45	FSRQ	-	0.724745	Albareti et al. (2017)
J1217+3007	ON 325	HBL	15.58	0.131	Nieppola et al. (2006)
J1221+3010*	1ES 1218+304	EHBL	16.8	0.18	Chang et al. (2019)
J1221+2813	W Comae	IBL	14.84	0.102	Nieppola et al. (2006)
J1224+2436	MS 1221.8+2452	HBL	15.68	0.219	Zhou et al. (2021)
J1224+2122	PKS 1222+21	FSRQ	-	0.433826	Albareti et al. (2017)
J1230+2518	ON 246	IBL	15.0	0.135	Chang et al. (2019)
J1415+1320	PKS 1413+135	LBL	13.4	0.247	Readhead et al. (2021)
J1422+3223	OQ 334	FSRQ	-	0.681	Abazajian et al. (2009)
J1427+2348	OQ 240	HBL	15.7	0.647	Nieppola et al. (2006)
J1428+4240*	1ES 1426+428	EHBL	18.1	0.129	Chang et al. (2019)
J1443+1200*	1ES 1440+122	EHBL	17.7	0.16	Chang et al. (2019)
J1443+2501	PKS 1441+25	FSRQ	-	0.939	Shaw et al. (2012)
J1518-2731	TXS 1515-273	HBL	15.3	0.14	Chang et al. (2019)
J1555+1111	PG 1553+113	HBL	15.6	0.36	Chang et al. (2019)
J1653+3945*	Mrk 501	EHBL	17.9	0.03	Chang et al. (2019)
J1725+1152	H 1722+119	HBL	16.46	0.180	Zhou et al. (2021)
J1728+5013*	IZw 187	EHBL	17.0	0.055	Chang et al. (2019)
J1743+1935*	1ES 1741+196	EHBL	17.8	0.08	Chang et al. (2019)
J1751+0938	PKS 1749+096	LBL	13.1	0.322	Abdo et al. (2010)
J1813+3144	B2 1811+31	FSRQ	15.0	0.117	Chang et al. (2019)
J1943+2118	HESS J1943+213	EHBL	18.1	0.22	Chang et al. (2019)
J1958-3011	1RXS J195815.6-301119	EHBL	17.0	0.119	Chang et al. (2019)
J1959+6508*	1ES 1959+650	EHBL	16.9	0.047	Chang et al. (2019)
J2001+4352	MAGIC J2001+435	HBL	~16	0.18	Aleksić et al. (2014)
J2039+5219*	1ES 2037+521	HBL	16.2	0.053	Zhou et al. (2021)
J2056+4940	RGB J2056+496	EHBL	17.6	0.1	Chang et al. (2019)
J2158-3013	PKS 2155-304	HBL	15.4	0.117	Chang et al. (2019)
J2202+4216	BL Lac	LBL	13.6	0.069	Abdo et al. (2010)
J2243+2021	RGB J2243+203	EHBL	15.1	-	Chang et al. (2019)
J2250+3825	B3 2247+381	HBL	16.33	0.119	Zhou et al. (2021)
J2347+5142*	1ES 2344+514	EHBL	17.7	0.044	Chang et al. (2019)

^aFor some sources, no redshift was found in the given reference. In these cases, if available, the redshift value was taken from either SIMBAD (<http://simbad.u-strasbg.fr/simbad/>) or NED (<https://ned.ipac.caltech.edu/>). For two sources, the redshift is still undetermined or disputed.

*EHBL sources overlapping with Biteau et al. (2020). † Observations are coordinated with the MOMO program (Komossa et al. 2023).

Table 2: Gain curve parameters used for the different receivers of the Effelsberg 100-m telescope

Receiver	A_0	$A_1 \times 10^3$	$A_2 \times 10^5$
20 mm	0.971	1.833	-2.867
14 mm	0.962	-1.950	-2.493
7 mm (36–39 GHz)	0.835	8.312	-10.46
7 mm (41–44 GHz)	0.785	11.26	-14.75

2.3.1. Sub-scan fitting

As mentioned in Sect. 2.2, every scan of a source at a specific frequency consists of multiple sub-scans. These sub-scans are used to calculate one flux density value for each frequency per scan. For every scan, all azimuth sub-scans are used to generate a single average azimuth scan and all elevation sub-scans are used to generate a single average elevation scan. Since all of the sample sources are assumed to be point-like and the primary beam/point spread function (PSF) of the telescope is well described by a 2D Gaussian, a Gaussian curve is fitted to both average scans. This fitting process is carried out with the `toolbox` software (Kraus et al. 2003). At this point, it is necessary to perform a data quality check to see if all sub-scans can be considered clean scans. This is important, since some sub-scans might be corrupted by radio frequency interference (RFI), telescope errors, or atmospheric effects, and therefore might lead to errors in the derived flux density values.

In order to filter out corrupted sub-scans, a flagging system has been developed, which uses multiple criteria to detect corrupted scans. The detailed flagging criteria are listed in Appendix A. If an averaged scan is flagged according to these criteria, it is not trivial to judge whether the source was below the detection limit (not visible in all sub-scans) or if there were simply a few corrupted sub-scans without checking every single sub-scan for every source. As done by Angelakis et al. (2019) a manual analysis of individual sub-scans is possible but very tedious, time-consuming, and also not clearly reproducible since it depends on the analyzer’s individual eyes. Therefore, we have developed a semi-automated analysis tool which takes care of detecting and sorting-out corrupted sub-scans. The general principle of the algorithm is presented in Appendix A. The automated analysis quality is superior to the manual analysis since every sub-scan deletion can be tried out, instead of simply judging by the human eye what sub-scan deletion might improve the overall fit quality. On top of that, due to the appointed flagging criteria, it is completely reproducible. As a final check, the data are again inspected manually to sort out any outliers and left-over corrupted scans, which the algorithm was not able to detect.

2.3.2. Data corrections

All averaged scans that passed our semi-automated flagging algorithm undergo further data reduction processes. These data reduction are composed of the pointing offset correction, atmospheric opacity correction, and elevation-dependent gain correction presented by Angelakis et al. (2019) in their Sect. 4. The only difference is that we determine the zenith opacity τ using a water-vapor radiometer located at the focus cabin of the telescope by measuring the strength of the 22 GHz water-vapor line (Roy et al. 2004). On top of that, we use updated gain curve parameters A_i as presented in Table 2.

2.4. Calibration

2.4.1. Calibrator sources

In this section, it is discussed how the calibration factor for the analysis is determined. Baars et al. (1977) have introduced a set of secondary calibrators that can be used on a day-to-day basis for calibration purposes. Their flux density is very constant over long periods of time (several decades) and they are also very compact sources. These secondary calibrators have been further investigated and monitored by Ott et al. (1994) and most lately by Perley & Butler (2013, 2017). According to the latest publication (Perley & Butler 2017), the best suited calibrators in the TELAMON frequency range (14 GHz–44 GHz) are 3C 286 and 3C 295. They are therefore used as calibrator sources in this work. Perley & Butler (2017) provide parametrized spectra for these sources that are used to calculate the frequency dependent calibrator flux densities for our analysis. Since 3C 295 is quite faint ($\lesssim 1$ Jy) at higher frequencies ($\nu \gtrsim 35$ GHz) and therefore not always detectable (especially during bad weather sessions), the sources NGC 7027 and W3(OH) are also included as calibrator sources. NGC 7027 is a planetary nebula and has been proposed as a secondary calibrator by Baars et al. (1977). Even though its flux density is gradually fading with time, this source can be used as a calibrator since its behavior has been well characterized by Zijlstra et al. (2008). The spectral model provided in this paper is used to calculate time-dependent calibration flux densities for NGC 7027. W3(OH) is a star forming region that exhibits a strong water maser in the 14 mm band (Hachisuka et al. 2006). Therefore, it is excluded for 14 mm calibration, but since the source is very bright at 7 mm (≈ 3 Jy) it is useful as a substitute for 3C 295 in this band. For W3(OH) we use our own calibration model which was created using Effelsberg archival data and assuming a free-free emission model. Due to their brightness, the two main calibrators observed with highest priority are 3C 286 and NGC 7027. 3C 295 is used as a backup calibrator at 20 mm and 14 mm, and W3(OH) as a backup calibrator at 20 mm and 7 mm. For one epoch in 2021, we used 3C 138 as a calibrator for all bands, using the Perley & Butler (2017) model.

2.4.2. Calibration process

As mentioned in Sect. 2.2, usually one of the secondary calibrator sources are observed every four hours during an observing session to determine the calibration factor. This calibration measurement typically consists of up to three scans per frequency on the calibrator. Usually, more than one scan of the calibrator is taken during a calibration measurement, therefore the mean and standard deviation are calculated to get a value with uncertainty for the calibration factor at the given time. In the case of only one calibrator measurement per calibration measurement the uncertainty is estimated depending on the frequency (see Sect. 2.5). For each observing session, one therefore gets a calibration factor for every ~ 4 hours, in the ideal case. An example is given in Fig. 1, where all calibration factor data points (black dots) are averages of the underlying (multiple) calibrator scans at the time. When talking about calibration factors in the following, it is referred to these, already (sub-)averaged calibration factors like the (black) ones presented in Fig. 1.

In principle, the calibration factor only depends on the sensitivity of the telescope at a given frequency and should therefore be constant throughout an observing session (for a given frequency). As one can see in Fig. 1 this is not always the case. The

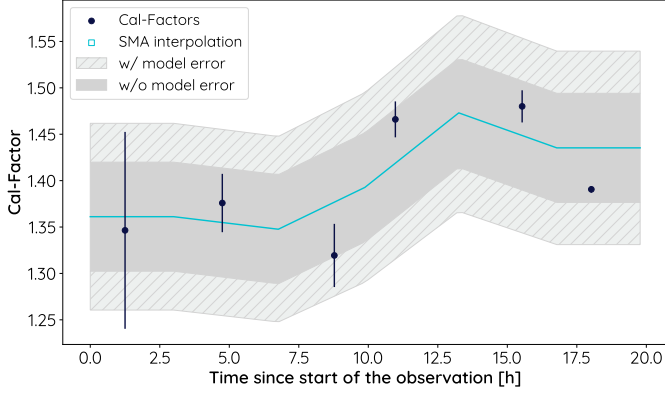


Fig. 1: An example of the calibration factor evolution at 38.75 GHz during the observing session on Oct 24, 2021. The black dots correspond to the (sub-)averaged calibration factor measurements $\Gamma_{c,i}$. The blue line and blue squares indicate the simple moving average (SMA) interpolated calibration factor $\Gamma_{\text{SMA},i}$ (see Equation (1)), as used in the final analysis. The dark gray area represents the calibrator scatter $\sigma_{\text{sc},\nu}$, while the light gray hashed area represents the total calibration uncertainty σ_{cal} , including the model uncertainty σ_{model} and $\sigma_{\text{sc},\nu}$.

calibration factor does change throughout the observing session, mostly due to temperature changes, which affect the ideal focus position. If the telescope is out of focus, the received signal is weaker and therefore the calibration factor rises. The telescope is being kept in focus by readjusting the focus every four hours (or more often in the case of significant temperature changes) to keep the calibration factor constant, but still the calibration factor varies throughout the observation. Modelling the behaviour of the focus is non-trivial, since it is unknown how much of the calibration factor fluctuation is statistical and how much is systematic due to, e.g., shifting focus. If the fluctuation was solely statistical, one would have to take the mean calibration factor throughout the entire session. If the fluctuation was solely systematic it would be best to linearly interpolate between the calibration factors. In the present case, however, interpolation between all data points would be an over-interpretation of the data and taking the mean cannot account for the fluctuation of the calibration factor. In order to take this fluctuation into account and also not to over-interpret the data points, the calibration factor is modelled by using a simple moving average (SMA) interpolation (Chou 1975). Essentially, this approach is a combination of both methods, since first, we take the mean between two adjacent calibration factor values and then interpolate between these mean values. If the calibration factor at time t_i is $\Gamma_{c,i}$, the interpolated values are calculated via

$$\Gamma_{\text{SMA},i} = \frac{\Gamma_{c,i} + \Gamma_{c,i+1}}{2}, \quad (1)$$

where $\Gamma_{c,i+1}$ is the calibration factor adjacent to $\Gamma_{c,i}$. The same procedure is used for the time interpolation

$$t_{\text{SMA},i} = \frac{t_i + t_{i+1}}{2}. \quad (2)$$

If initially there are n calibration factors $\Gamma_{c,i}$, this interpolation will result in $n - 1$ interpolated calibration factors $\Gamma_{\text{SMA},i}$. As indicated by the blue line in Fig. 1, we interpolate linearly between the $(t_{\text{SMA},i}, \Gamma_{\text{SMA},i})$ values to get a general expression for the calibration factor at any given time. For times $t < t_{\text{SMA},1}$, the calibration factor is modelled as constant $\Gamma_{\text{SMA},1}$. Analogously, for

times $t > t_{\text{SMA},n-1}$, the calibration factor is modelled as constant $\Gamma_{\text{SMA},n-1}$. If there is only one or two calibration factors available ($n = 1, 2$), a constant calibration factor is assumed for the entire epoch. For all other cases, the interpolation (blue line) is used to determine the calibration factor at any given time during the observing session. This means, for every source scan, one calculates the corresponding calibration factor Γ_c using the SMA-interpolation and then uses this calibration factor to calculate the flux density of the source S_{source} via

$$S_{\text{source}} = T_{\text{src}} \cdot \Gamma_c, \quad (3)$$

where T_{src} is the observed source temperature.

2.5. Discussion of uncertainties

In this section, we discuss the determination of the total flux density uncertainties σ_{tot} . The final uncertainty has to include the main uncertainties due to the sub-scan fitting process with the data corrections σ_{fit} , and the uncertainty of the calibration factor, σ_{cal} .

First, we focus on the uncertainty due to sub-scan fitting and data corrections, σ_{fit} . Its value is calculated through Gaussian error propagation from the fitting and data correction process explained in Sect. 2.3.2. Note that the gain curve is assumed to be free of uncertainty here, since the accuracy of the gain curve is also reflected in the fluctuation of the calibration factors and therefore included in the calibration uncertainty σ_{cal} . Usually, atmospheric corrections have the biggest impact on the data correction uncertainty, especially in sessions affected by bad weather. In total, σ_{fit} is on average on the order of $\sim 1\%$.

The main contribution of the flux density uncertainties comes from the calibration uncertainty, σ_{cal} . There are two sources of uncertainty that determine the total calibration uncertainty. First, one needs to consider the fluctuation of the calibration factor $\sigma_{\text{sc},\nu}$ for each frequency and observing epoch. Secondly, one needs to account for the uncertainty of the underlying calibrator model σ_{model} . As explained in the previous section, an SMA-interpolation is used to calculate interpolated calibration factors. To be conservative, the uncertainty of the interpolated calibration factors is assumed to be constant. Therefore, the standard deviation (RMSD) of all (non-interpolated) calibration factors for each frequency and observing epoch is used as the uncertainty

$$\sigma_{\text{sc},\nu} = \sqrt{\frac{1}{n-1} \sum_{i=1}^n (\Gamma_{c,i} - \bar{\Gamma}_c)^2}. \quad (4)$$

Here, $\bar{\Gamma}_c$ is the mean over the non-interpolated calibration factors $\Gamma_{c,i}$. This uncertainty is also illustrated in Fig. 1 by the dark gray background. In the case where only one calibration factor was measured during an observing epoch, it is non-trivial to determine a sensible value for this uncertainty. In order to deal with this special case, the calibration factor scattering for each frequency from all observing epochs has been analyzed. An illustrative plot of the calibration factor evolution at 41.25 GHz throughout the entire program since August 2020 is shown in Fig. 2. In order to derive a sensible uncertainty for these epochs, the standard deviation of all calibration factors throughout the program is used to get an estimate of the average calibration factor scatter. This analysis is performed for every frequency band. Following this procedure, a conservative calibration uncertainty of 5 % is used at 20 mm and 14 mm and 10 % at 7 mm for epochs with only one calibration factor. In Fig. 2, one can also see that

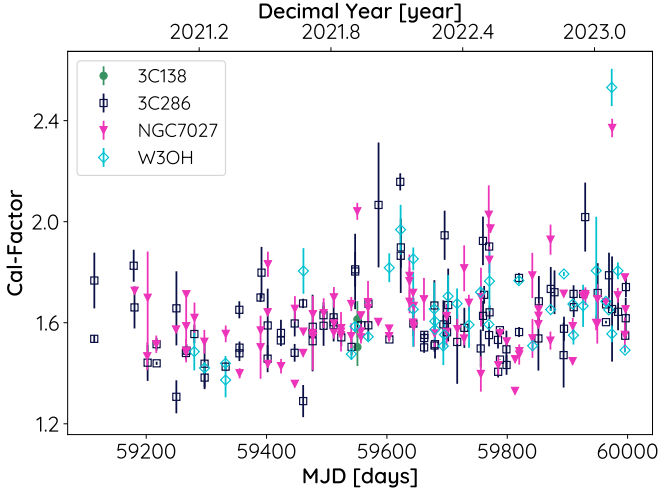


Fig. 2: Illustrative calibration factor evolution at 41.25 GHz throughout the entire program. We determine the calibration factor scattering uncertainty $\sigma_{sc,v}$ by taking the standard deviation of these values at each frequency. In this example, $\sigma_{sc,v}$ is on the order of 10 %. Significant outliers can be explained by bad weather epochs.

for some epochs the calibration factor varies more than for others. This is due to varying focus because of significant temperature and weather fluctuations (on shorter time scales than the usual focus adjustment interval every ~ 4 hours) in some observing sessions.

In addition to the calibration factor scattering $\sigma_{sc,v}$, one also needs to take into account the accuracy of the calibrator models σ_{model} . The models of 3C 295, 3C 138 and 3C 286 by Perley & Butler (2017) have an estimated accuracy of 3 % to 5 %, with the larger uncertainty at the lowest (~ 50 MHz) and highest (~ 50 GHz) ends. Since the observations take place from 14 GHz–44 GHz, which is at the higher end of their scale, an uncertainty of 5 % for the 3C 295, 3C 138 and 3C 286 models is assumed. For the timely variable model of NGC 7027, Zijlstra et al. (2008) provide an uncertainty of 6 %. It is estimated that the uncertainty for the W3(OH) model is also in the same range, since it has a similar underlying free-free emission model. As a conservative estimate, a general accuracy of the calibrator models of $\sigma_{model}/\Gamma_c = 6\%$ is assumed, which is the maximum uncertainty out of the models. One must not use the Gaussian law of error propagation to combine the uncertainties of the different models, since they are not statistically independent and all based on the same flux density scale by Baars et al. (1977). To calculate the total calibration uncertainty σ_{cal} , the estimated model uncertainty σ_{model} and the calibration scatter $\sigma_{sc,v}$, which is individual for every epoch and frequency, are added quadratically. The total calibration uncertainty is therefore given by

$$\sigma_{cal} = \sqrt{\sigma_{model}^2 + \sigma_{sc,v}^2}. \quad (5)$$

In order to obtain the total flux density uncertainty σ_{tot} , one needs to combine σ_{cal} with the fitting uncertainty σ_{fit} . This is done by Gaussian error propagation. Following Equation (3), one finds

$$\frac{\sigma_{tot}}{S_{source}} = \sqrt{\left(\frac{\sigma_{cal}}{\Gamma_c}\right)^2 + \left(\frac{\sigma_{fit}}{T_{src}}\right)^2} \quad (6)$$

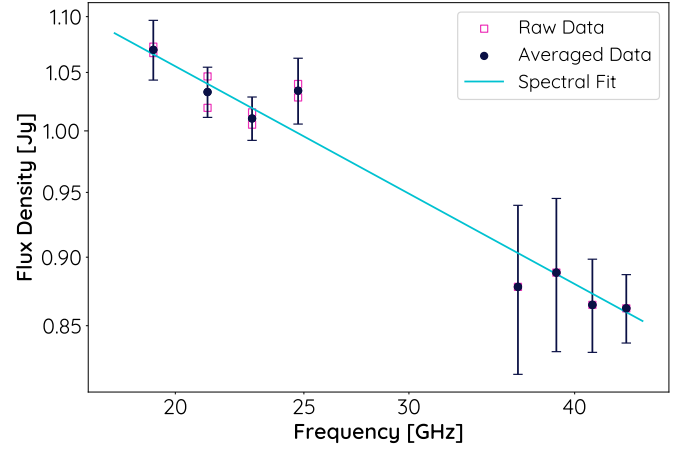


Fig. 3: Example of the spectral fitting process (J1653+3945, known as Mrk 501 on July 28, 2021). The magenta squares indicate the raw data, uncertainties are not shown to enhance readability. For every frequency, where more than one raw flux density value is available, the flux densities are averaged (black dots). The averaged flux densities are then fitted with a power-law spectrum (blue line). In the presented case, one finds $\alpha = -0.262 \pm 0.021$.

for the total flux density uncertainty. Note that for the following analysis the model uncertainty is considered to be zero, since it is purely systematic throughout the entire program. Using it would therefore lead to an overestimation of the statistical flux density uncertainty. If the presented flux density values were to be combined with other radio data (using a different flux density scale), or if the absolute flux density values are of interest, the model uncertainty has to be taken into account.

3. Results

3.1. Median spectral indices

In order to characterize the TELAMON TeV-sample in terms of the spectral index, we calculate spectral indices for every observation and present their medians in Table 3. For some sources there is no sufficient frequency coverage available (i.e., less than three individual frequencies detected). Therefore, we could determine a sensible spectral index for 43 of our sample sources.

3.1.1. Spectral index calculation

As established earlier, there can be two measurements of a source per epoch and frequency, which means that there exists more than one flux density value for the same frequency. This can be seen in the example presented in Fig. 3 (magenta squares). In this case, the average flux density per frequency is calculated by taking the mean. If there is only one flux density value per frequency available, it is used as-is. The averaged values are depicted as black dots in Fig. 3. The uncertainty is determined by Gaussian error propagation, since distinct scans are considered independent measurements. After this first averaging process, a spectral power-law fit is performed to the data for every source at every observed epoch. This power-law is defined via

$$S(\nu) \propto \nu^\alpha, \quad (7)$$

where S is the source flux density, ν the observed frequency and α the spectral index. The fit is performed using a Levenberg-

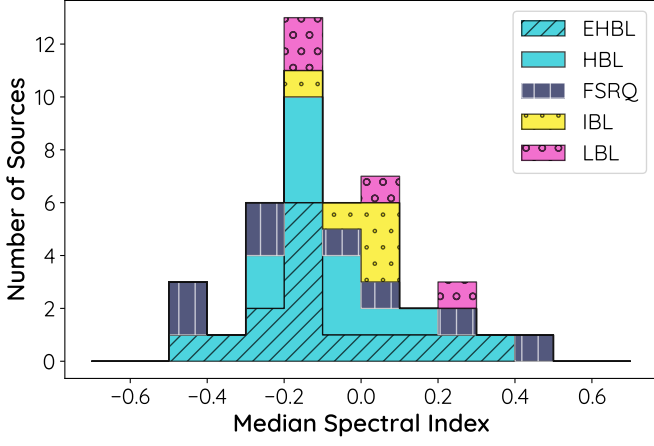


Fig. 4: Distribution of the median spectral index across all available bands (i.e., 14 GHz–45 GHz), as found in the TELAMON sample sources.

Marquardt fitting algorithm (Moré 1978). An example of such a fit for the source J1653+3945 (Mrk 501) on July 28, 2021 is shown in Fig. 3, which results in a spectral index $\alpha = -0.262 \pm 0.021$. This analysis is applied to the entire data set, where at least three sub-band detections across all receivers (i.e., 14 GHz–45 GHz) are available for the same epoch and source. In order to get a typical value for the spectral index for every source, we list their median spectral indices in Table 3, taken over all epochs. This is done only for sources for which spectral indices could be determined in three or more independent epochs to avoid outliers.

3.1.2. Spectral indices in the TELAMON sample

All median spectral indices across all bands (i.e., 14 GHz–45 GHz) are presented in Table 3, and in Fig. 4 as a histogram plot binned according to the source type. We find an overall average spectral index of -0.07 , with a standard deviation of 0.20 and a median of -0.11 . This is consistent with the expectation of a flat spectrum. We therefore conclude that the TeV-selected sub-sample of blazars presented here does not show any unexpected or special spectral features. In order to test if the spectral index distribution of HBL and EHBL is statistically different, we perform a two-sample Kolmogorov-Smirnov-test (KS-Test) which leads to a p-value of $p = 0.40$. This clearly indicates that the distributions cannot be distinguished and most likely have the same underlying statistics. For all other source classes, the sample size is not sufficient to perform significant statistical studies.

3.2. Average flux densities

In order to simplify the analysis, the observed flux densities of every source and epoch are averaged over the sub-frequencies of the 20 mm, 14 mm and 7 mm receivers, respectively. This means for every source we derive an average flux density value at 20 mm, 14 mm, and 7 mm for each epoch, given that the source was observed and the detected in these bands. The main reason for this is that in some cases not all of the four (two for 20 mm) sub-bands of each receiver show a significant source detection. This can be due to RFI, because the source is too weak at the highest frequencies, or due to background noise. Averag-

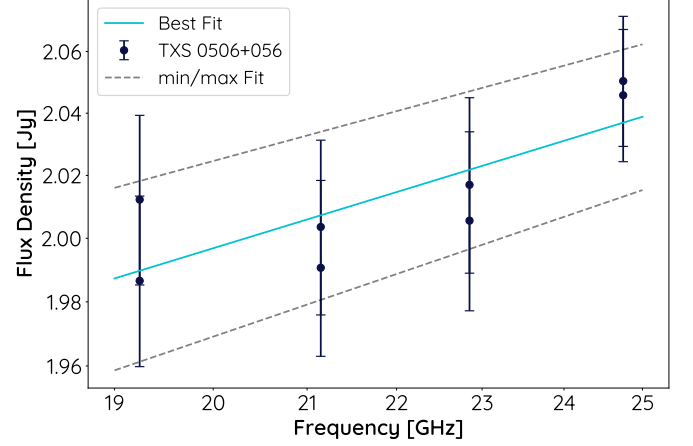


Fig. 5: Example of the sub-band averaging process (J0509+0541, known as TXS 0506+056 on Jan 2, 2021 at 14 mm). The average flux density is calculated by taking the integral of the best fit between 19 GHz and 25 GHz. The uncertainties are determined by integrating the min/max fits.

ing over the sub-bands of each receiver will make it possible to compare all epochs with each other, even if a sub-band flux density value might be vacant in one or more epochs. However, taking the mean or the weighted mean of all measured values does not suffice to ensure the comparability of epochs. For example, if a source was detected at 19.25 GHz and 21.15 GHz at Epoch A and at another Epoch B at 22.85 GHz and 24.75 GHz, taking the mean will shift the mean frequency of this average. Since the spectrum of the sample sources is not always flat ($S(\nu) \neq \text{const.}$), this could turn out to be problematic when comparing flux densities from two distinct epochs. We therefore introduce a new method of obtaining average flux densities from the receiver sub-bands using spectral fits in the following section.

3.2.1. Sub-band averaging

For each receiver (7 mm, 14 mm and 20 mm), at first a power-law spectral fit (cf. Eq. (7)) is performed to the raw data within the receiver band width. Similar to the spectral index calculation in Sect. 3.1.1, a Levenberg-Marquart fitting algorithm is used to calculate the fit. Note that here, we set a bound of $|\alpha| < 0.5$ to the spectral index, since the analysis presented here is more sensitive to outliers. From the fit, the average flux density \bar{S} in the range of the receiver bandwidth is calculated:

$$\bar{S} = \frac{\int_{\nu_1}^{\nu_2} S(\nu) d\nu}{\nu_2 - \nu_1}. \quad (8)$$

For the 20 mm receiver, the integration limits are $\nu_1 = 14$ GHz and $\nu_2 = 17$ GHz, for the 14 mm receiver $\nu_1 = 19$ GHz and $\nu_2 = 25$ GHz, and for the 7 mm receiver $\nu_1 = 36$ GHz and $\nu_2 = 44$ GHz. This method ensures that the average flux density is always calculated from the same frequency range, with best knowledge about the intrinsic spectrum of the source for each epoch. In the case where data for only one sub-frequency (e.g., only for 19.25 GHz) are available, it is not possible to perform a sensible fit. In these cases, a flat spectrum ($\alpha = 0$) is assumed, since this is typical for the sources in the sample (e.g., Zensus 1997).

In order to define an uncertainty for the average flux density values, different approaches are used according to how many

Table 3: Average flux densities for all sources from the TELAMON sample as observed during the first 2.5 years. The median spectral index has been calculated across all receiver bands and epochs. Detection rates and the number of epochs each source was observed are shown.

ID (J2000)	$S_{20\text{mm}}^a$ [Jy]	D-Rate ^b [%]	N_{obs}^c	$S_{14\text{mm}}^a$ [Jy]	D-Rate ^b [%]	N_{obs}^c	$S_{7\text{mm}}^a$ [Jy]	D-Rate ^b [%]	N_{obs}^c	α^d
J0035+5950	0.0725 ± 0.0074	88	18	0.0676 ± 0.0055	85	14	-	0	4	-0.35
J0112+2244	-	-	0	1.47 ± 0.36	95	48	1.57 ± 0.42	93	47	0.10
J0136+3906	0.0413 ± 0.0051	83	6	0.0397 ± 0.0022	100	1	-	-	0	-
J0152+0146	-	0	3	-	-	0	-	-	0	-
J0214+5144	0.167 ± 0.012	93	15	0.151 ± 0.015	82	23	0.162 ± 0.014	12	8	-0.42
J0221+3556	-	-	0	0.609 ± 0.043	95	21	0.465 ± 0.063	100	21	-0.44
J0222+4302	-	-	0	0.94 ± 0.12	100	30	0.82 ± 0.17	86	29	-0.18
J0232+2017	0.0413 ± 0.0051	79	24	0.0377 ± 0.0074	52	25	-	0	4	0.32
J0316+4119	0.1386 ± 0.0070	94	17	0.135 ± 0.013	86	30	-	0	12	-0.15
J0319+1845	0.0202 ± 0.0021	50	2	-	0	1	-	-	0	-
J0416+0105	0.0535 ± 0.0081	85	20	0.051 ± 0.010	68	19	-	0	6	-0.16
J0507+6737	0.0278 ± 0.0013	25	4	0.0277 ± 0.0016	22	9	-	0	2	-
J0509+0541	-	-	0	1.33 ± 0.43	97	40	1.17 ± 0.41	89	39	-0.12
J0521+2112	-	-	0	0.373 ± 0.029	97	33	0.366 ± 0.048	74	31	0.01
J0648+1516	0.0324 ± 0.0064	100	1	0.0312 ± 0.0024	100	1	-	-	0	-
J0650+2502	0.0879 ± 0.0082	77	18	0.0860 ± 0.0099	85	21	-	0	4	-0.13
J0710+5909	0.05440 ± 0.00042	20	10	0.0452 ± 0.0022	100	1	-	-	0	-
J0721+7120	-	-	0	0.83 ± 0.17	100	8	0.79 ± 0.19	87	8	-0.04
J0733+5153	0.0704 ± 0.0069	22	9	-	-	0	-	-	0	-
J0739+0136	-	-	0	1.55 ± 0.34	100	10	1.70 ± 0.35	70	10	0.03
J0809+5219	0.146 ± 0.011	80	10	0.135 ± 0.014	90	10	-	0	1	-0.02
J0812+0237	0.0403 ± 0.0050	70	17	0.0438 ± 0.0095	50	6	-	-	0	-
J0847+1133	-	0	2	-	0	1	-	-	0	-
J0854+2006	-	-	0	6.03 ± 0.93	100	9	5.6 ± 1.1	88	9	-0.12
J0958+6533	-	-	0	1.90 ± 0.30	80	10	2.49 ± 0.61	88	9	0.43
J1015+4926	0.243 ± 0.014	92	14	0.224 ± 0.014	90	22	0.215 ± 0.041	33	6	-0.24
J1058+2817	0.095 ± 0.011	83	18	0.100 ± 0.011	77	18	-	0	1	0.19
J1104+3812	0.465 ± 0.021	100	2	0.424 ± 0.046	95	45	0.419 ± 0.062	67	40	-0.05
J1136+7009	0.1628 ± 0.0057	86	15	0.151 ± 0.020	88	25	-	0	7	-0.23
J1136+6737	0.0350 ± 0.0040	77	9	-	0	1	-	-	0	-
J1159+2914	-	-	0	4.5 ± 2.1	100	10	4.9 ± 2.2	80	10	-0.07
J1217+3007	0.374 ± 0.024	100	2	0.404 ± 0.050	96	32	0.410 ± 0.059	89	29	-0.05
J1221+3010	0.0555 ± 0.0064	93	16	0.065 ± 0.016	75	12	-	0	2	0.28
J1221+2813	0.521 ± 0.052	50	2	0.490 ± 0.056	94	39	0.458 ± 0.065	75	36	-0.10
J1224+2122	-	-	0	0.89 ± 0.15	90	10	0.624 ± 0.078	88	9	-0.49
J1224+2436	0.0324 ± 0.0087	90	10	-	-	0	-	-	0	-
J1230+2518	0.2639 ± 0.0049	100	1	0.342 ± 0.063	93	30	0.369 ± 0.092	84	26	0.05
J1415+1320	0.657 ± 0.021	100	2	0.564 ± 0.066	87	16	0.54 ± 0.12	80	15	-0.13
J1422+3223	0.675 ± 0.023	100	2	0.73 ± 0.18	94	39	0.81 ± 0.22	91	37	0.21
J1427+2348	0.416 ± 0.042	100	1	0.362 ± 0.051	100	32	0.335 ± 0.073	60	30	-0.11
J1428+4240	0.0304 ± 0.0046	33	6	0.0225 ± 0.0021	7	14	-	0	2	-
J1443+1200	0.0403 ± 0.0035	77	9	0.0417 ± 0.0060	100	1	-	-	0	-
J1443+2501	0.260 ± 0.057	86	29	0.221 ± 0.057	97	34	-	0	4	-0.26
J1555+1111	0.368 ± 0.035	92	27	0.339 ± 0.043	97	42	0.313 ± 0.061	50	14	-0.01
J1653+3945	1.187 ± 0.034	100	2	1.057 ± 0.051	100	35	0.885 ± 0.085	84	32	-0.27
J1725+1152	0.116 ± 0.015	90	10	0.125 ± 0.028	90	10	-	-	0	0.18
J1728+5013	0.127 ± 0.010	90	21	0.123 ± 0.015	91	34	-	0	11	-0.11
J1743+1935	0.208 ± 0.015	90	20	0.191 ± 0.015	100	33	-	0	11	-0.19
J1751+0938	2.25 ± 0.33	100	6	2.35 ± 0.39	100	13	2.43 ± 0.51	100	13	0.07
J1813+3144	0.106 ± 0.010	83	18	0.1070 ± 0.0099	92	27	-	0	4	-0.21
J1943+2118	0.0377 ± 0.0076	61	18	0.0316 ± 0.0022	11	9	-	-	0	-
J1959+6508	0.204 ± 0.019	90	21	0.197 ± 0.017	86	36	0.2122 ± 0.0091	18	11	-0.15
J2001+4352	0.223 ± 0.056	100	14	0.230 ± 0.053	100	14	-	-	0	0.05
J2039+5219	0.0285 ± 0.0039	100	1	-	0	1	-	-	0	-
J2056+4940	0.117 ± 0.018	77	9	0.111 ± 0.017	66	9	-	-	0	-0.13
J2202+4216	-	-	0	5.8 ± 2.3	90	11	7.1 ± 2.7	90	11	0.27
J2250+3825	-	0	2	-	-	0	-	-	0	-
J2243+2021	0.0987 ± 0.0058	70	20	0.0988 ± 0.0087	78	19	-	-	0	0.04
J2347+5142	0.1615 ± 0.0097	90	20	0.151 ± 0.014	87	33	-	0	12	-0.29

^aAverage flux density and standard deviation at the given wavelength taken over all observed epochs. ^bDetection rate (i.e., number of epochs with detection divided by the number of epochs where the source was observed) at the given wavelength. ^cNumber of epochs where the source was observed at the given wavelength. ^dMedian spectral index across all observed epochs with at least three sub-band detections. ^eSource was observed but not detected at 20 mm and 14 mm. We have confirmed with independent 45 mm observations that the source is indeed very faint, i.e., a successful detection at wavelengths < 20 mm is unlikely. For these faint sources we have defined a new observing category and are now monitoring them with high detection rates at 45mm.

sub-bands are detected. In the case of two, three or four (i.e., all) sub-frequencies detected, two additional (uncertainty-)fits are performed: One with the uncertainties subtracted from the measured flux density values and the other one with the uncertainties added to the measured values (min- and max-fit). This is justified since in this case, the uncertainty mostly consists of systematic calibration uncertainty, i.e., the measured values may all together be higher (or lower) than the best values but relative to each other, they are known much more precisely. This procedure is illustrated in Fig. 5. The uncertainty is determined by the difference between the best fit to the minimum and maximum flux density (min/max-fit), and the best fit to the flux density value. In the case of only one sub-frequency detected, this is vastly different, since no sensible fit can be performed. The uncertainty of this value is estimated in a similar manner to the min/max-fits mentioned earlier. Again, the measurement uncertainties are subtracted/added to the flux density value. Then, different spectral distributions with $\alpha \in \{-0.5; 0; 0.5\}$, originating at the min/max flux densities, are considered. This means, one gets three alternate spectral distributions for minimum and maximum flux density, respectively. Analogous to the previous calculations, the difference between the integrated alternate spectral distributions and the integrated best fit (in this case the flat spectrum) is calculated. The maximum difference is then used as the average flux density uncertainty.

In the following sections, when referring to flux densities at 7 mm, 14 mm or 20 mm, we always refer to the sub-band-averaged flux density in each band, calculated using the method introduced in this section, if not declared otherwise.

3.2.2. Flux densities in the TELAMON sample

The sub-band averaging procedure introduced in the previous section provides us with one flux density value at 20 mm, 14 mm and 7 mm for every source at every epoch, given that it was observed and detected. In order to get an overview of the general source properties, we calculate the average flux densities of every source for 20 mm, 14 mm and 7 mm over time from the sub-band averaged flux densities. This allows us to characterize the observed sample in terms of average source flux density. All average flux density values are presented in Table 3. Their uncertainties correspond to the standard deviation of the sub-band averaged flux densities and therefore also reflect the intrinsic source variability. In the case where a source has only been detected once, the presented uncertainty is equal to the uncertainty of the sub-band averaged flux density. All average flux densities presented in Table 3 are also depicted as histogram plots in Fig. 6, binned according to the source type. Here, one can see that the 7 mm flux densities (Fig. 6, bottom) are by far the smallest sample and limited to flux densities ≥ 150 mJy. Only 25 out of 41 observed sources show a significant detection at 7 mm. This can be explained by the detection limit of the 7 mm receiver (see Sect. 4.3) and by the fact that most of the sources in our sample are too faint to be detected at 7 mm. This is vastly different at 20 mm and 14 mm. At 14 mm (Fig. 6, center), 51 of the 55 observed sources show a significant detection in at least one epoch. At 20 mm (Fig. 6, top), 44 of the 47 observed sources show a significant detection in at least one epoch. Only three observed sources (J0152+0146, J0847+1133, J2250+3825) have not been detected at all. We have confirmed with independent 45 mm observations that these sources are amongst the faintest in our sample and therefore most likely below the detection limit of the telescope at shorter wavelengths with the current setup.

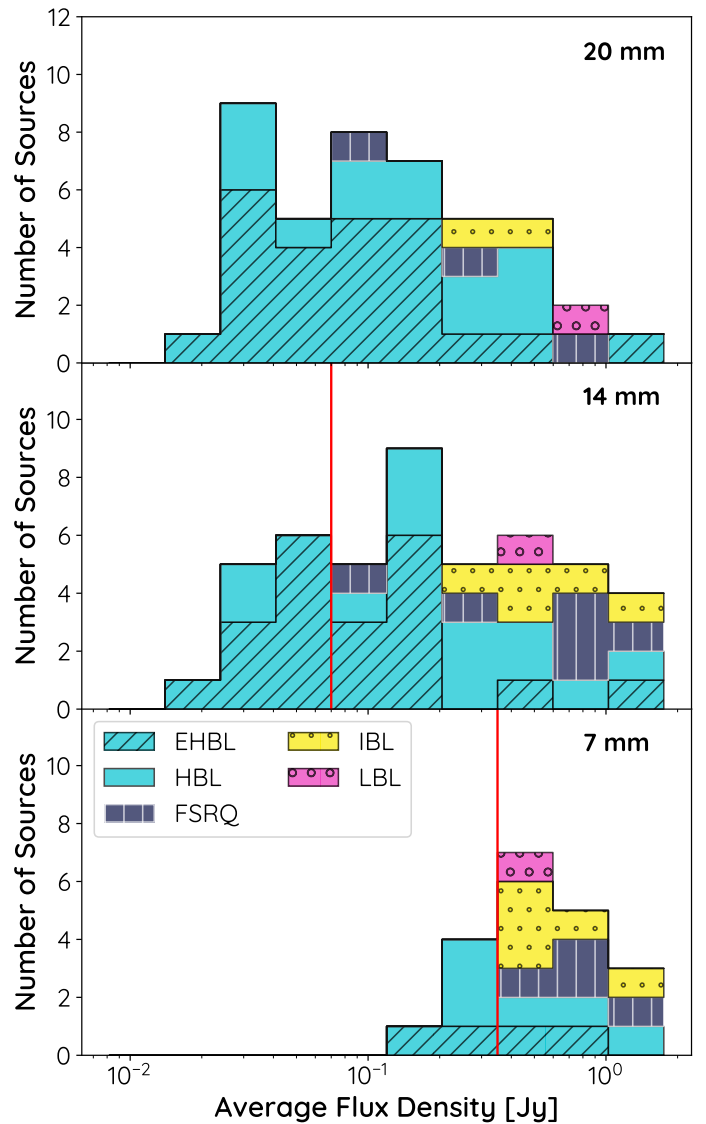


Fig. 6: Distribution of the average flux density found in the TELAMON sample sources for the 20 mm (top), 14 mm (center), and 7 mm (bottom) receivers. The histogram is divided into the source classes EHBL (blue with diagonal stripes), HBL (blue), IBL (yellow with dots), LBL (magenta with circles) and FSRQ (black with vertical stripes). The red vertical lines indicate the flux density above which one can expect a $> 50\%$ detection chance per epoch (see Sect. 4.3). Below these thresholds the statistics are significantly affected due to the limited telescope sensitivity. For 20 mm we do not have enough data on the faintest sources to determine this limit.

Following from the values presented in Table 3, we find an average 7 mm flux density of 1.4 Jy with a standard deviation of 1.8 Jy and a median of 0.6 Jy in our sample. This can only be considered as an upper limit to the average 7 mm flux density of the entire sample, since it is heavily biased by the non-detection of sources with flux densities ≤ 150 mJy due to the sensitivity limit at 7 mm. At 14 mm, the average source flux density is 0.7 Jy with a standard deviation of 1.3 Jy and a median of 0.2 Jy. At 20 mm, we find an average source flux density of 0.24 Jy with a standard deviation of 0.38 Jy and a median of 0.12 Jy. At the latter two wavelengths, the receiver sensitivity also limits the detection of very faint sources, but since almost all sources from our sample

were detected in these bands, we consider this bias to be much less significant than for 7 mm. This allows us to perform a sensible statistical comparison of the 20 mm and 14 mm data. For both wavelengths, we find that according to a two sample KS-test one cannot reject the null-hypothesis that EHBL and HBL have the same underlying statistical distribution (14 mm: $p = 0.06$; 20 mm: $p = 0.34$). However, the sub-sample of EHBLs seems to populate lower flux densities than the sub-sample of HBLs according to the median average flux densities. At 20 mm, the subsample of EHBLs exhibits a median average flux density of 0.071 Jy, while for HBLs one finds a median of 0.15 Jy. At 14 mm, the subsample of EHBLs exhibits a median average flux density of 0.10 Jy, while for HBLs one finds a median of 0.22 Jy. In summary, the sub-sample of HBLs shows higher flux densities than the sub-sample of EHBLs in both bands. This is consistent with the per definition higher synchrotron peak frequencies of EHBLs and the blazar sequence (Fossati et al. 1998; Donato et al. 2001) which suggests that sources become fainter in the radio band with increasing synchrotron peak frequency.

3.3. Detection rates

In order to analyze the impact of the receiver sensitivity on the detectable source flux density, we calculate detection rates for all observed sources and receivers. For every source, we count the observing epochs (dates) during which the source was observed and the epochs where the source was detected in at least one sub-frequency of the given receiver. The detection rate is then given by the number of detections divided by the number of observations. The detection rates and number of observations for each receiver and source are presented in Table 3 next to the average flux density values. These detection rates are further discussed in section 4.3.

4. Discussion

In this section, we discuss and compare the TELAMON source properties with previous programs, namely the F-GAMMA monitoring (Fuhrmann et al. 2016; Liidakis et al. 2017; Angelakis et al. 2019) and a study on TeV-selected blazars by Lindfors et al. (2016).

4.1. Spectral index discussion

Since the study by Lindfors et al. (2016) was carried out only at a single radio frequency (15 GHz), we can only compare spectral indices with the F-GAMMA program. Angelakis et al. (2019) provide spectral indices for various frequency windows, however, none of them is comparable with the TELAMON spectral range (i.e., 15 GHz–44 GHz). We have therefore used light curves provided by Angelakis et al. (2019) to derive spectral indices similar to Sect. 3.1.1, but only taking into account flux density values for frequencies 14.6 GHz, 23.05 GHz, 32 GHz and 43 GHz to ensure comparability between the derived spectral indices for TELAMON and F-GAMMA. Note that the F-GAMMA data (Angelakis et al. 2019) includes several (non-blazar) sources with a steep spectrum ($\alpha \lesssim -0.8$), which the TELAMON sample does not show. These are mostly calibrator sources which we exclude for further discussion. Figure 7 shows a direct comparison of the distribution of both samples in form of a histogram plot. The overall sample size of F-GAMMA (91 sources with spectral index) is superior to the TELAMON sample (43 sources with spectral index). According to a two-

sample KS-test, we find that the samples most likely have the same underlying distributions ($p = 0.11$). This suggests that GeV-emitting blazars and TeV-emitting blazars exhibit similar spectral indices.

4.2. Flux density discussion

Similar to the spectral index comparison, we have calculated average flux densities for the F-GAMMA data at 23.05 GHz from Angelakis et al. (2019) to compare with the TELAMON average flux densities at the overlapping wavelength of 14 mm. On top of that, we use the average flux density values provided by Lindfors et al. (2016) at 15 GHz for an additional comparison. All three flux density distributions are depicted in Fig. 8. One can clearly see that the flux densities of the GeV-selected F-GAMMA sources are in general much higher than for the TeV-selected Lindfors et al. (2016) and TELAMON samples. This is consistent with the fact that most TeV emitting blazars have their SED shifted to higher energies and are consequently fainter in the radio band. We further performed a two-sample KS-test to compare TELAMON flux densities with the F-GAMMA and Lindfors et al. (2016) sample and find with high significance that the TELAMON and Lindfors et al. (2016) sources show a similar distribution ($p = 0.30$) while we have to reject the null-hypothesis of similar underlying distributions for TELAMON and F-GAMMA ($p = 1.4 \times 10^{-16}$). We therefore conclude that this difference in flux density seems to be characteristic for the target selection of either GeV- (F-GAMMA) or TeV-selected (TELAMON, Lindfors et al. 2016) blazars. TeV-emitting blazars seem to be fainter radio emitters than GeV-emitting blazars. Note that all three programs are limited by similar telescope sensitivity, which means we expect that this has no impact on the statistical comparison of the samples.

4.3. Long-term monitoring strategy

In order to address the question of the telescope sensitivity limit and to suggest a TeV-blazar sample well suited for long-term monitoring observations with the Effelsberg 100-m telescope, we discuss the relationship between source flux density and detection rate for all three receivers (20 mm, 14 mm and 7 mm) in this section. One can see in Table 3 that for some very faint sources the detection rate is rather low (i.e., $\sim 10\%$). Observing these sources in a long-term monitoring study would lead to a waste of telescope time that could instead be used to include other (brighter) sources with better detection potential more frequently. On top of that, in order to perform variability and multi-wavelength correlation studies, a sufficient sample size (flux density measurements per source) is required, which would take decades for sources with low detection rates and an observing cadence of two to four weeks. Moreover, such a sensitivity study can be useful to derive upper flux density limits in case of a non-detection in future studies.

In principle, the detection rate should only depend on the sensitivity of the receiver and can be calculated by telescope intrinsic parameters. However, given that we are performing a long-term monitoring program, bad weather epochs and intrinsic source variability can influence the detectability of fainter sources, especially at the highest frequencies. To maximize source detections, we try to prioritize the faintest sources during good weather conditions, but this is not always possible since we are trying to keep a cadence of two to four weeks for all sources. In principle, the detection chances for the faintest sources can

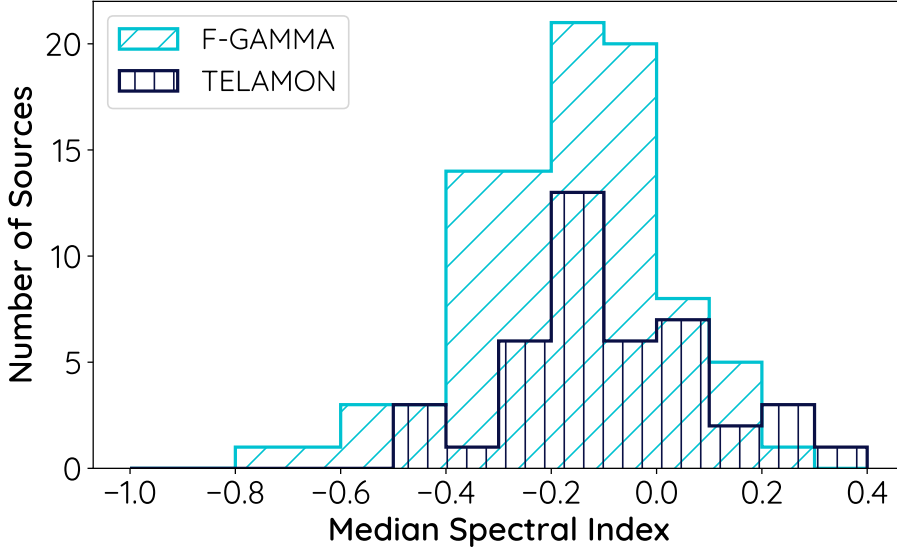


Fig. 7: Histogram plot of median spectral indices for all sources from the F-GAMMA sample (Angelakis et al. 2019, blue with diagonal stripes) and the TELAMON (black with vertical stripes) sample between 14 GHz and 45 GHz.

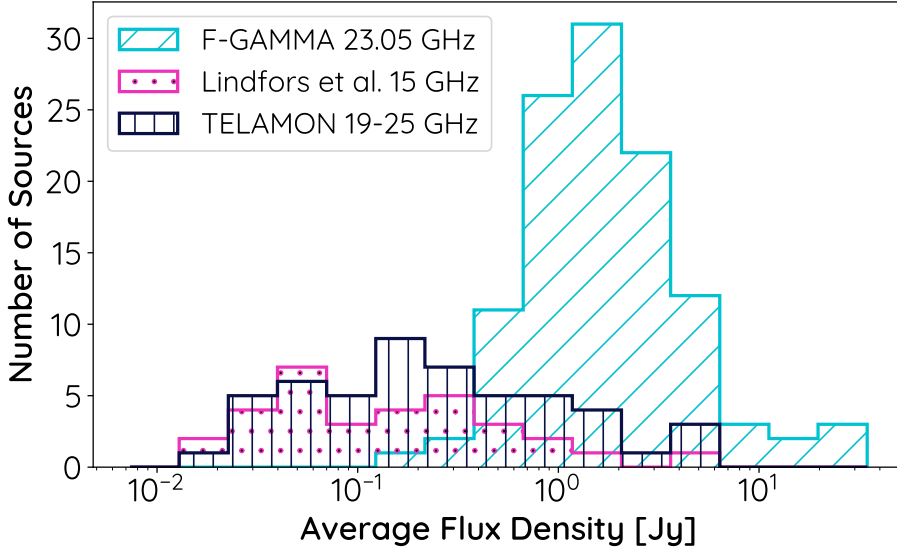


Fig. 8: Comparison of the GeV-selected F-GAMMA (Angelakis et al. 2019, blue with diagonal stripes) and the TeV-selected Lindfors et al. (2016) and TELAMON samples (magenta with dots and black with vertical stripes, respectively) according to the average source flux density (F-GAMMA: 23.05 GHz, Lindfors et al.: 15 GHz, TELAMON: 14 mm, i.e., 19 GHz–25 GHz).

be increased by using more scans, i.e., spending more observing time per source. However, due to the limited observing time and large number of sources this was usually not feasible. We consider the 2.5 year observations presented in this paper to be a good representation of such effects and therefore well suited to identify a flux density limit above which it is sensible to monitor sources as part of a long-term study with the given telescope and observing setup. For each receiver, we calculate the average detection rate for all sources below a certain flux density threshold. This is done for 10,000 different flux density thresholds. Moreover, this entire procedure is carried out 1,000 times with varying average source flux densities in a Monte-Carlo (MC) way, assuming the average flux densities and their uncertainties in Table 3 correspond to Gaussian distributions. The mean average detection rate and its standard deviation taken from the 1,000 MC-iterations is then plotted in Fig. 9 for 10,000 different flux density threshold values. In order to guarantee statistical convergence, we require a minimum of three sources to be included in the average detection rate count, therefore the average detection rates in Fig. 9 can only be presented above a certain flux density threshold. If we assume that the detection rate is mono-

tonically increasing with flux density, the detection rate curves in Fig. 9 correspond to lower limits of the actual detection rate at any given flux density. For a sensible long term monitoring, we require a minimum detection rate of 50 % (i.e., a source detection at least every other epoch) to optimize the scientific outcome of the observing time and to prevent too many non-detections. Using the data from Fig. 9, we can determine a flux density limit S_0 for each receiver above which we expect a detection rate of at least 50 %. For the 14 mm receiver, we find $S_0 = 70.8^{+8.3}_{-6.3}$ mJy, and for 7 mm $S_0 = 337^{+36}_{-50}$ mJy. For the 20 mm receiver, we do not have enough data on the faintest sources to determine a flux density threshold for a detection rate of 50 %. All sources with a 20 mm flux density $\gtrsim 30$ mJy have a detection chance > 50 %.

Sources below a 20 mm flux density of ~ 30 mJy have a limited detection chance with either of the three introduced receivers. We therefore started observing these sources at even longer wavelengths (i.e., 45 mm, sub-sample I) to have the best chances to detect them in our long-term monitoring program. The second faintest sources, exhibiting a 20 mm flux density $\gtrsim 30$ mJy but a 14 mm flux density $\lesssim 70$ mJy, are monitored at 20 mm (sub-sample II) in the current observing setup. Brighter

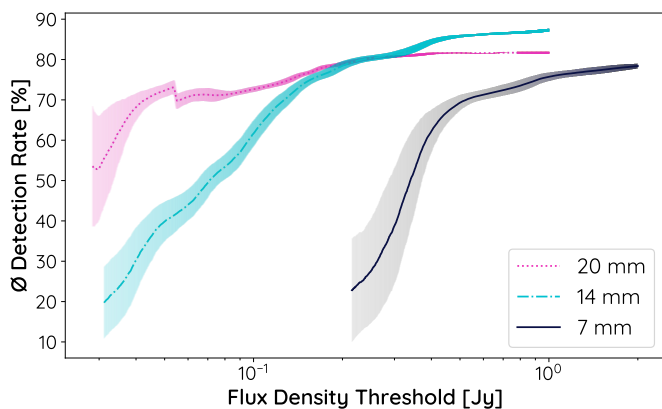


Fig. 9: Average detection rate for sources below a given flux density threshold for the 20 mm, 14 mm and 7 mm receiver as calculated from the first 2.5 years of TELAMON observations. The errors are calculated in a Monte-Carlo way, which takes into account the variability of the observed sources.

sources ($S_{14\text{mm}} \gtrsim 70 \text{ mJy}$ and $S_{7\text{mm}} \lesssim 350 \text{ mJy}$) can be monitored at 20 mm and 14 mm (sub-sample III) in a sensible way, and for the brightest sources ($S_{7\text{mm}} \gtrsim 350 \text{ mJy}$) sensible monitoring is possible at both 14 mm and 7 mm (sub-sample IV). Note that in principle these thresholds can be improved by spending more time on each source, i.e., performing more sub-scans. However, this tactic is not favorable for our program, since we need to establish an ideal trade-off between observing time spent per source and the total number of sources that can be monitored. In Fig. 10, we show example light curves of one representative source per sub-sample. One can see in light curves (a), (b), and (c), that we tried monitoring the sources with higher frequency receivers than suggested by the sub-sample, which resulted in fairly low detection rates. Since the adaption of the sub-samples, the detection rates have significantly improved. Ongoing TELAMON observation are conducted according to this strategy as it is the best possible setup for our purposes.

5. Conclusions & outlook

We have presented the first results of the pilot-phase (August 2020 - February 2023) of the TELAMON AGN monitoring program for a complete sample of all TeV-emitting blazars in the Northern Hemisphere. We have used the Effelsberg 100-m telescope to monitor these sources at high radio frequencies from 14 GHz–44 GHz every two to four weeks. We have developed a semi-automated data reduction pipeline which allows for immediate reduction of the data. From the observations, we derived flux densities and spectral indices from the sources in our sample. Plots of the latest available light curves and source spectra are publicly available on the dedicated TELAMON website⁴.

Our results are consistent with the findings of a prior study of the same object class by Lindfors et al. (2016). In comparison to the GeV-selected F-GAMMA sample (Fuhrmann et al. 2016; Angelakis et al. 2019), we find that the spectral indices of both GeV- and TeV-selected sources are consistent with a flat spectrum. The average flux density at 14 mm is significantly lower in the TeV-selected sample than what Angelakis et al. (2019) have found in their study. The comparison between GeV- and TeV-emitting blazars is still limited by the small number of TeV-

emitting blazars, which is expected to increase within the next years with upcoming observations from the Cherenkov Telescope Array (Mazin 2019).

In future studies, we will analyze the variability of TeV-blazars and perform correlation studies with multi-wavelength light curves, similar to previous studies of GeV-emitting AGN (e.g., Paraschos et al. 2023; Rösch et al. 2022; Fuhrmann et al. 2014). For several individual sources we have already demonstrated the multi-wavelength capabilities of our program (e.g., Gokus et al. 2022; Menezes et al. 2021), especially in combination with our complementary Southern Hemisphere monitoring program at the Australia Telescope Compact Array (e.g., Eppel et al. 2023). Moreover, the TELAMON program will continue its observations using an optimized observing setup including measurements at 45 mm for very faint radio sources. In addition, we will provide results on follow-up observations of neutrino-candidate blazars, which have not been discussed in this paper. Another publication reporting on the polarization properties of our TeV-sample is currently in preparation (cf. Heßdörfer et al. 2023).

Acknowledgements. This work is based on observations with the 100-m telescope of the MPIfR (Max-Planck-Institut für Radioastronomie) at Effelsberg. FE, SH, JH, MK and FR acknowledge support from the Deutsche Forschungsgemeinschaft (DFG, grants 447572188, 434448349, 465409577). We acknowledge the M2FINDERS project from the European Research Council (ERC) under the European Union’s Horizon 2020 research and innovation programme (grant agreement No 101018682).

References

- Abazajian, K. N., Adelman-McCarthy, J. K., Agüeros, M. A., et al. 2009, *ApJS*, 182, 543
- Abdo, A. A., Ackermann, M., Agudo, I., et al. 2010, *ApJ*, 716, 30
- Aharonian, F., Akhperjanian, A. G., Barres de Almeida, U., et al. 2008, *A&A*, 481, L103
- Ahn, C. P., Alexandroff, R., Allende Prieto, C., et al. 2012, *ApJS*, 203, 21
- Ahnen, M. L., Ansoldi, S., Antonelli, L. A., et al. 2017, *A&A*, 603, A25
- Albaret, F. D., Allende Prieto, C., Almeida, A., et al. 2017, *ApJS*, 233, 25
- Aleksić, J., Ansoldi, S., Antonelli, L. A., et al. 2014, *A&A*, 572, A121
- Aleksić, J., Antonelli, L. A., Antoranz, P., et al. 2011, *ApJ*, 729, 115
- Aliu, E., Aune, T., Beilicke, M., et al. 2011, *ApJ*, 742, 127
- Angelakis, E., Fuhrmann, L., Myserlis, I., et al. 2019, *A&A*, 626, A60
- Baars, J. W. M., Genzel, R., Pauliny-Toth, I. I. K., & Witzel, A. 1977, *A&A*, 500, 135
- Becerra González, J., Acosta-Pulido, J. A., Bosch, W., et al. 2021, *MNRAS*, 504, 5258
- Biteau, J., Prandini, E., Costamante, L., et al. 2020, *Nature Astronomy*, 4, 124
- Chang, Y. L., Arsioli, B., Giommi, P., Padovani, P., & Brandt, C. H. 2019, *A&A*, 632, A77
- Chou, Y.-I. 1975, *Statistical Analysis* (Holt, Rinehart & Winston of Canada Ltd.)
- Ciprini, S., Tosti, G., Teräsranta, H., & Aller, H. D. 2004, *MNRAS*, 348, 1379
- Costamante, L., & Ghisellini, G. 2002, *A&A*, 384, 56
- Donato, D., Ghisellini, G., Tagliaferri, G., & Fossati, G. 2001, *A&A*, 375, 739
- Eppel, F., Kadler, M., Ros, E., et al. 2023, *IAU Symposium*, 375, 91
- Fossati, G., Maraschi, L., Celotti, A., Comastri, A., & Ghisellini, G. 1998, *MNRAS*, 299, 433
- Fuhrmann, L., Angelakis, E., Zensus, J. A., et al. 2016, *A&A*, 596, A45
- Fuhrmann, L., Larsson, S., Chiang, J., et al. 2014, *MNRAS*, 441, 1899
- Ghisellini, G. 1999, *Astroparticle Physics*, 11, 11, *TeV Astrophysics of Extragalactic Sources*
- Giommi, P., Glauch, T., Padovani, P., et al. 2020, *MNRAS*, 497, 865
- Giommi, P., Massaro, E., Chiappetti, L., et al. 1999, *A&A*, 351, 59
- Gokus, A., Kreikenbohm, A., Leiter, K., et al. 2022, in *37th International Cosmic Ray Conference*, 869
- Grasha, K., Darling, J., Bolatto, A., Leroy, A. K., & Stocke, J. T. 2019, *ApJS*, 245, 3
- Hachisuka, K., Brunthaler, A., Menten, K. M., et al. 2006, *ApJ*, 645, 337
- Heßdörfer, J., Kadler, M., Benke, P., et al. 2023, *arXiv e-prints*, arXiv:2309.14794
- Hillas, A. M. 1984, *ARA&A*, 22, 425
- Kadler, M., Bach, U., Berge, D., et al. 2021, *PoS, ICRC2021*, 974
- Komossa, S., Kraus, A., Grupe, D., et al. 2023, *ApJ*, 944, 177

⁴ <https://telamon.astro.uni-wuerzburg.de/>

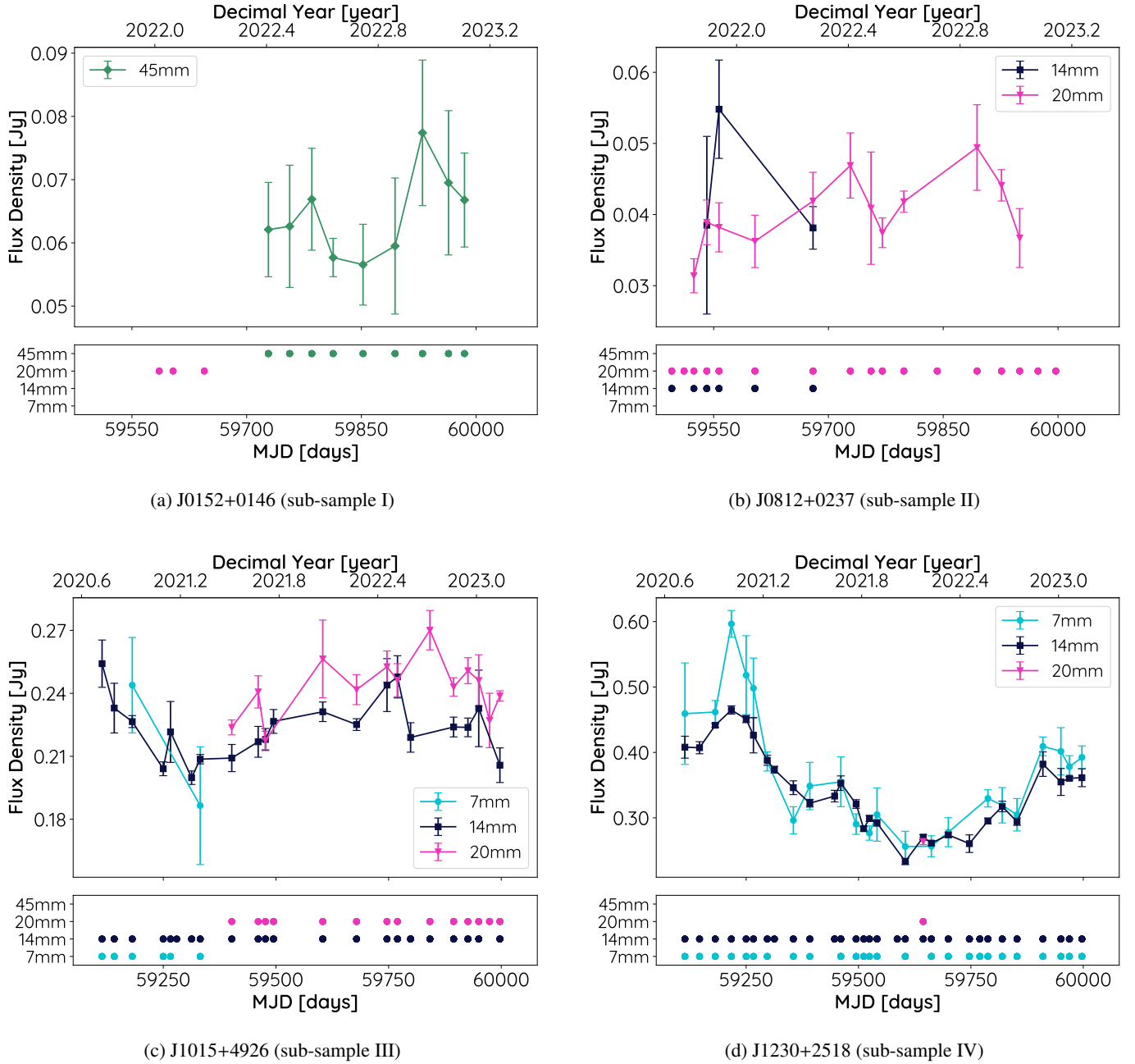


Fig. 10: Illustrative light curves (upper panels) of four selected sources from the TELAMON TeV-sample. The flux densities are averaged over the individual receiver sub-bands as described in Sect. 3.2.1. The lower panels indicate the times of observation with the given receiver. If there is no matching flux density at the same time in the light curve, the source was not detected.

Kraus, A., Krichbaum, T. P., Wegner, R., et al. 2003, *A&A*, 401, 161
 Lindfors, E. J., Hovatta, T., Nilsson, K., et al. 2016, *A&A*, 593, A98
 Liodakis, I., Marchili, N., Angelakis, E., et al. 2017, *MNRAS*, 466, 4625
 Mannheim, K. 1995, *Astroparticle Physics*, 3, 295
 Mazin, D. 2019, in *International Cosmic Ray Conference*, Vol. 36, 36th International Cosmic Ray Conference (ICRC2019), 741
 Menezes, R. et al. 2021, *PoS, ICRC2021*, 955
 Moré, J. J. 1978, in *Numerical Analysis*, ed. G. A. Watson (Berlin, Heidelberg: Springer Berlin Heidelberg), 105–116
 Müller, P., Krause, M., Beck, R., & Schmidt, P. 2017, *A&A*, 606, A41
 Nieppola, E., Tornikoski, M., & Valtaoja, E. 2006, *A&A*, 445, 441
 Ott, M., Witzel, A., Quirrenbach, A., et al. 1994, *A&A*, 284, 331
 Padovani, P. & Giommi, P. 1995, *ApJ*, 444, 567
 Padovani, P., Petropoulou, M., Giommi, P., & Resconi, E. 2015, *MNRAS*, 452, 1877
 Paiano, S., Landoni, M., Falomo, R., et al. 2017, *ApJ*, 837, 144
 Paraschos, G. F., Mpisketzis, V., Kim, J. Y., et al. 2023, *A&A*, 669, A32

Perley, R. A. & Butler, B. J. 2013, *ApJS*, 204, 19
 Perley, R. A. & Butler, B. J. 2017, *ApJS*, 230, 7
 Readhead, A. C. S., Ravi, V., Liodakis, I., et al. 2021, *ApJ*, 907, 61
 Rösch, F., Kadler, M., Ros, E., et al. 2022, in *European VLBI Network Mini-Symposium and Users' Meeting 2021*, Vol. 2021, 1
 Roy, A. L., Teuber, U., & Keller, R. 2004, in *European VLBI Network on New Developments in VLBI Science and Technology*, 265–270
 Shaw, M. S., Romani, R. W., Cotter, G., et al. 2012, *ApJ*, 748, 49
 Tavecchio, F., Ghisellini, G., & Guetta, D. 2014, *ApJ*, 793, L18
 Ventura, S., Prandini, E., Fallah Ramazani, V., et al. 2021, in *43rd COSPAR Scientific Assembly*. Held 28 January - 4 February, Vol. 43, 1281
 Zensus, J. A. 1997, *ARA&A*, 35, 607
 Zhou, R. X., Zheng, Y. G., Zhu, K. R., & Kang, S. J. 2021, *ApJ*, 915, 59
 Zijlstra, A. A., van Hoof, P. A. M., & Perley, R. A. 2008, *ApJ*, 681, 1296

Appendix A: Flagging criteria for sub-scan fitting

As mentioned in Sect. 2.3.1, we apply different criteria to check for corrupted scans in our data analysis pipeline. The general data pipeline procedure is illustrated in Fig. A.1. A scan is flagged if at least one of the following criteria applies:

- The full-width at half maximum (FWHM) of the Gaussian fit of either the azimuth or elevation or both average scans deviates by more than 30% from the frequency dependent half power beam width (HPBW). *Reason: The FWHM of a point-source scan is restricted by the angular resolution limit (beam width), depending on the observing frequency. Therefore, it should stay constant for each frequency and not vary significantly from source to source. There can be small positional telescope uncertainties throughout the sub-scans that lead to a slightly different FWHM of the averaged source scan, but these changes should not exceed $\sim 30\%$. This flag type is typical for windy observing sessions, where the telescope's position changes slightly from sub-scan to sub-scan by wind gusts, or in cases where the source is below the detection limit and only background noise is fitted.*
- The Gaussian fit of either azimuth or elevation or both average scans has negative amplitude. *Reason: The sources are expected to be point-like radio emitters, this means one expects to observe a Gaussian signal with a positive peak in total intensity. Since a negative amplitude indicates a dip in the Gaussian, there is something wrong with one or more sub-scans. It can also indicate that the source is below the detection limit and not visible at all, i.e., only background noise is fitted.*
- The maximum of the Gaussian fit of either azimuth or elevation or both average scans has an offset from the scan center greater than 20% of the HPBW. *Reason: The Gaussian fit is expected to be centered in azimuth and elevation scans. If this is not the case, the cross-scan has missed the source position by several arcseconds. In principle, these cases are corrected in the analysis (see Sect. 2.3.2), but at a level of more than 20% of the beam width this offset correction is not accurate anymore.*
- The amplitudes of the Gaussian fits of azimuth and elevation average scans differ by more than 15%. *Reason: The source is expected to be point-like and centered in azimuth and elevation scans. This means the average scans in azimuth and elevation should have similar amplitudes. If amplitudes differ by more than 15% this is an indication of corrupted sub-scans included in the average scan or of the cross-scan not being centered at the source position.*

Note that the exact limits that indicate when a scan is flagged rely on experience. The chosen values have proven to be well suited for the analysis in the used frequency bands. For every scan (usually consisting of 8 or 16 sub-scans), it is first checked if the averaged scan is flagged. If the scan is not flagged, it will be used as-is for the next analysis steps without performing any changes. If the scan is flagged, the algorithm tries to remove one sub-scan and checks if the average scan (excluding the removed sub-scan) is still flagged. If this new average scan is not flagged, the average scan, excluding the deleted sub-scan, will be used for further analysis steps. If the new average scan is still flagged this procedure goes on until the algorithm has found a combination of removed sub-scans that leads to a non-flagged average scan. The algorithm allows for up to two sub-scans in total to be removed from the initial scan. If the average scan is still flagged after trying to remove all sub-scan combinations, the scan is sorted out as a corrupted scan and it is not used for further analysis.

Appendix B: Results on additional TeV-sources

For the statistical analysis in sections 3 and 4 we have excluded the five Southern TeV-blazars, which were monitored in the beginning of the program, and the radio galaxy J1145+1936 (3C 264). Their average flux densities and 14 mm average spectral indices are presented in Table ???. For consistency, we have re-run all statistical tests that we performed in sections 3 and 4 including the five Southern TeV-blazars. We find that our results and conclusions are not significantly impacted. The similarity of F-GAMMA and TELAMON spectral indices becomes more significant ($p = 0.19$), and the difference of HBLs and EHBLs within the TELAMON sample becomes slightly more significant at 20 mm ($p = 0.07$) and 14 mm ($p = 0.01$). We chose not to include these five sources in the main analysis since they are not chosen randomly and would introduce a statistical bias to the otherwise complete sample of all TeV-detected blazars in the Northern Hemisphere.

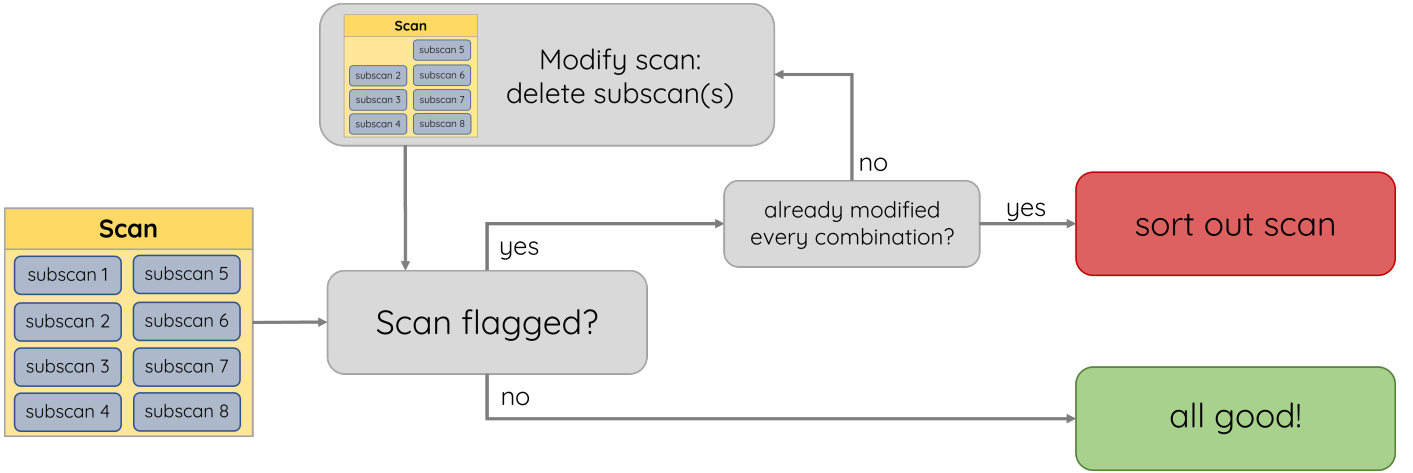


Fig. A.1: Flow diagram of the (semi-)automated flagging algorithm to sort out corrupted scans (cf. Sect.2.3.1)

Table B.1: Average flux densities for all five Southern sources from the TELAMON sample and the TeV-detected radio galaxy J1145+1936 (3C 264) as observed during the first 2.5 years. The median spectral index has been calculated across all receiver bands and epochs. Detection rates and the number of epochs each source was observed are shown.

ID (J2000)	$S_{20\text{ mm}}^a$ [Jy]	D-Rate ^b [%]	N_{obs}^c	$S_{14\text{ mm}}^a$ [Jy]	D-Rate ^b [%]	N_{obs}^c	$S_{7\text{ mm}}^a$ [Jy]	D-Rate ^b [%]	N_{obs}^c	α^d
J0303–2407	0.201 ± 0.015	90	10	0.185 ± 0.023	88	18	-	0	7	-0.38
J0913–2103	0.1459 ± 0.0049	71	7	0.1201 ± 0.0038	83	6	-	-	0	-0.42
J1518–2731	0.220 ± 0.032	80	5	0.207 ± 0.020	77	9	-	0	3	-0.30
J1958–3011	0.07635 ± 0.00049	66	3	0.100 ± 0.014	33	3	-	-	0	-
J2158–3013	0.369 ± 0.050	71	7	0.352 ± 0.063	69	13	-	0	6	-0.19
J1145+1936	0.484 ± 0.033	94	18	0.341 ± 0.027	96	26	0.224 ± 0.012	28	7	-0.91

^a Average flux density and standard deviation at the given wavelength taken over all observed epochs. ^b Detection rate (i.e., number of epochs with detection divided by the number of epochs where the source was observed) at the given wavelength. ^c Number of epochs where the source was observed at the given wavelength. ^d Median spectral index across all observed epochs with at least three sub-band detections.